

6

Coherent Beam Combining and Atmospheric Compensation with Adaptive Fiber Array Systems

Mikhail Vorontsov, Thomas Weyrauch, Svetlana Lachinova, Thomas Ryan, Andrew Deck,
Micah Gatz, Vladimir Paramonov, and Gary Carhart

6.1

Introduction

One of the most promising technologies that may dramatically change traditional laser beam transmitter (beam director) systems is related with recent advances in *coherent combining* of beams (beamlets) that are generated in a multichannel optical power amplifier (MOPA) fiber system and transmitted through a coupled MOPA array of fiber collimators [1–7]. In the directed energy (beam projection) applications considered here, coherent beam combining implies phasing of the outgoing beamlets at a remotely located target in the atmosphere by controlling their piston phases at the fiber collimator subapertures. Ideal target plane phasing of N_{sub} outgoing beamlets results in their constructive interference leading potentially to an N_{sub} -fold increase of combined beam target plane peak intensity, compared to incoherent beam combining in the absence of beamlets' phasing [3–6]. Note that coherent beam combining can only be achieved if the outgoing beamlets are quasi-monochromatic and have identical (or nearly identical) polarization states and spatial mode structure [1,4]. These requirements are fulfilled in a so-called *coherent fiber array system* based on a narrow-line seed laser and polarization-maintaining (PM), single-mode fiber elements and subsystems. A notional schematic of a coherent fiber array-based laser beam projection system is shown in Figure 6.1. In this system, control of piston phases at the fiber array pupil plane is performed using an optoelectronic target-in-the-loop (TIL) feedback system [7–9]. This control system includes a bistatic optical receiver that transforms the captured target return wave power into an electric signal J_{PIB} known as the power-in-the-bucket (PIB) metric, a metric processor that computes a phase-locking control metric J , and a phase-locking controller that utilizes the metric signal for computation of control voltages (controls) $\{u_j\}, j = 1, 2, \dots, N_{\text{sub}}$. Phase shifters that are integrated into the MOPA system transform the control voltages $\{u_j\}$ into optical wave time delays, resulting in controllable changes of the outgoing beam phases averaged over the fiber collimator subaperture areas, which are referred to as *piston phases*. The

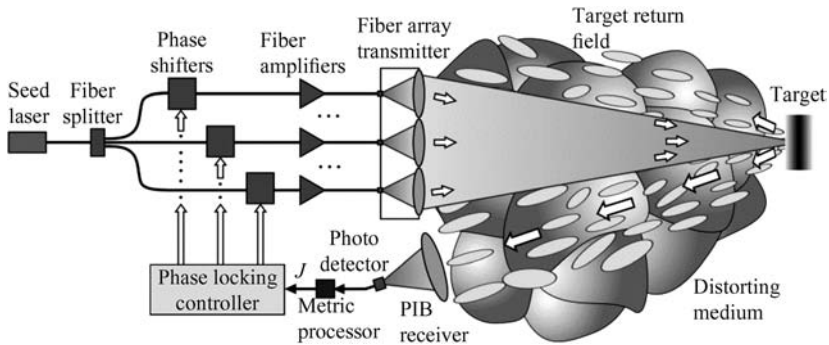


Figure 6.1 Notional schematic of a laser beam projection system based on coherent phased fiber array technology.

transmitted beamlets form a *combined beam* that propagates to the target. Atmospheric turbulence-induced refractive index inhomogeneities result in scintillations of the projected combined beam intensity inside the illuminated target area (target hit spot) and a decrease in the average projected beam power density (target hit spot brightness).

Achievement of the smallest (ideally, diffraction-limited) target hit spot in the vicinity of an assigned target aim point – the ultimate goal in the directed energy applications – requires precise overlapping of the transmitted beamlets, also referred to here as *combined beam focusing*, fine combined beam pointing and stabilization, and real-time compensation of both the MOPA system-induced random phase shifts and atmospheric turbulence-induced phase aberrations. In this chapter, we describe recent results of basic research in the area of fiber array system development with major focus on fiber array architectures, integration of adaptive optics (AO) and beam control capabilities, as well as coherent beam combining and atmospheric compensation techniques with the common goal of the projected beam power density increase at either unresolved (point source) or resolved (extended or speckle) targets.

6.2

Fiber Array Engineering

There are several considerations that impact the design of fiber collimator array-based beam directors. First, since in most applications the position of the target in space can be dynamically changing due to either target or beam director platform (or both) movement, the fiber array beam director should provide capabilities for the combined beam pointing and target hit spot stabilization in the conditions of changing beam propagation direction and distance. This requires integration of tracking, beam pointing, and beam focusing functions into the fiber array-based beam director. Similar to conventional beam directors based on laser transceiver telescopes with monolithic mirrors, target tracking and coarse beam pointing can be

performed by integrating the fiber array system into a gimbaled platform. Nevertheless, both fine beam pointing and hit spot stabilization require significantly higher accuracy than gimbals can provide. In conventional beam directors, the required accuracy is achieved by controlling the outgoing beam tip and tilt phase with relatively small size beam steering mirrors located in the beam director optical train prior to the final beam expansion with a transmitter telescope. In the case of fiber array-based systems, fine beam pointing can only be achieved with integration of tip and tilt wavefront phase control into each fiber collimator.

Second, in conventional systems, beam focusing is performed via displacement of the transmitter telescope secondary mirror, which leads to formation of a parabolic (spherical) wavefront phase of the outgoing beam. Since fiber array-based systems do not have external beam-forming optics, the combined beam focusing can be only performed using phase-shaping elements that are directly integrated into fiber collimators.

Consider the following two options for the integration of wavefront-shaping capabilities into the fiber collimator array, which can be utilized for the fine steering and focusing of the combined beam. The simplest option is related with approximation of tip-tilt and parabolic phase functions using subaperture-averaged (piston) phases, as illustrated in Figure 6.2a. This wavefront approximation, referred to as the *stair-mode approximation*, can be achieved using the fiber-integrated phase shifters of the MOPA system. A more accurate approximation of the combined beam phase can be obtained using, in addition to pistons, control of tip and tilt phase components at each fiber collimator subaperture (Figure 6.2b) [4]. As shown in Figure 6.2c, such tip-tilt control of the outgoing beamlet phase can be achieved using x and y displacements of the fiber tip that is located in the collimating lens focus. In the fiber-tip positioner devices that are specially developed for this purpose, displacements of the fiber tips are performed using piezoelectric actuators [7,10].

Examples of fiber array-based laser transmitters with integrated capabilities for piston and tip-tilt phase control at each fiber collimator aperture, developed by the authors, are shown in Figure 6.3. These fiber arrays have identical subaperture diameter d , subaperture fill factor $f_{\text{sub}} = d_0/d$, and the fiber array aperture fill factor f_c that is defined by the ratio $f_c = l/d$, where d_0 is the diameter of the Gaussian beam at the fiber collimator exit and l is the distance between the beamlets' optical axes [4]. The fiber array system, shown in Figure 6.3a and referred to here as the *fiber array cluster*, is composed of seven densely packed fiber collimators [11]. This fiber array cluster is envisioned as a building block (module) that can be used for increasing (scaling) the number of subapertures in the array by assembling together fiber array systems composed of several clusters, as illustrated in Figure 6.3b. A different approach to a fiber array system scaling is illustrated in Figure 6.3c. The increase in the number of subapertures from 7 to 19 is achieved here by incorporating the external chain of 12 additional fiber collimators into the fiber array cluster.

To estimate the potential benefits of integrating the wavefront phase tip-tilt control into individual fiber collimators, consider ideal target plane phasing in vacuum of the coherent fiber arrays in Figure 6.3 that utilize either solely piston

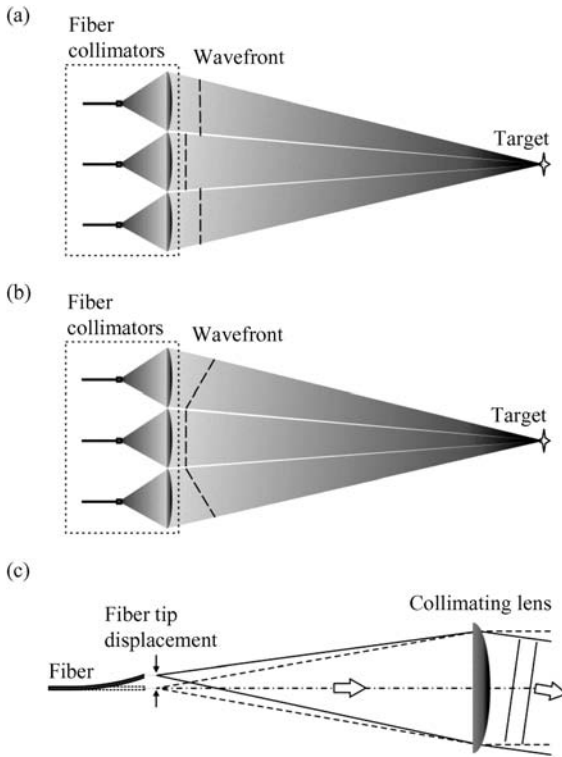


Figure 6.2 Combined beam focusing using (a) stair-mode and (b) piston and tip-tilt approximations of the parabolic wavefront. Tip and tilt control in each fiber collimator subaperture in (b) can be performed using displacement of the fiber tip, as shown in (c) [7,10].

(stair mode) or both piston and tip-tilt phase control at each fiber collimator subaperture. Spatial distributions of the combined beam power projected onto the target plane over a distance of 2 and 7 km are characterized in Figure 6.4 by the dependencies of the total power J_{PIB} inside the on-axis circular area (bucket), commonly referred to as the *target plane* PIB metric, on the bucket diameter d_T and by the corresponding target plane intensities shown as grayscale images on the right. For comparison, the PIB metrics for the seven-subaperture incoherent system are shown in Figure 6.4a by the dotted lines. Numerical calculations of the target plane intensity $I_T(\mathbf{r})$ were performed using Fresnel (parabolic) approximation of the diffraction theory [12,13]. As the results presented in Figure 6.4 suggest, the tip-tilt control allows the desired redirection of a portion of projected beam energy from the side lobes into the central (on-axis) lobe that is associated with the target hit spot. The expected benefit from the tip-tilt control is most pronounced for beam projections over relatively short distances and with increased number of subapertures N_{sub} .

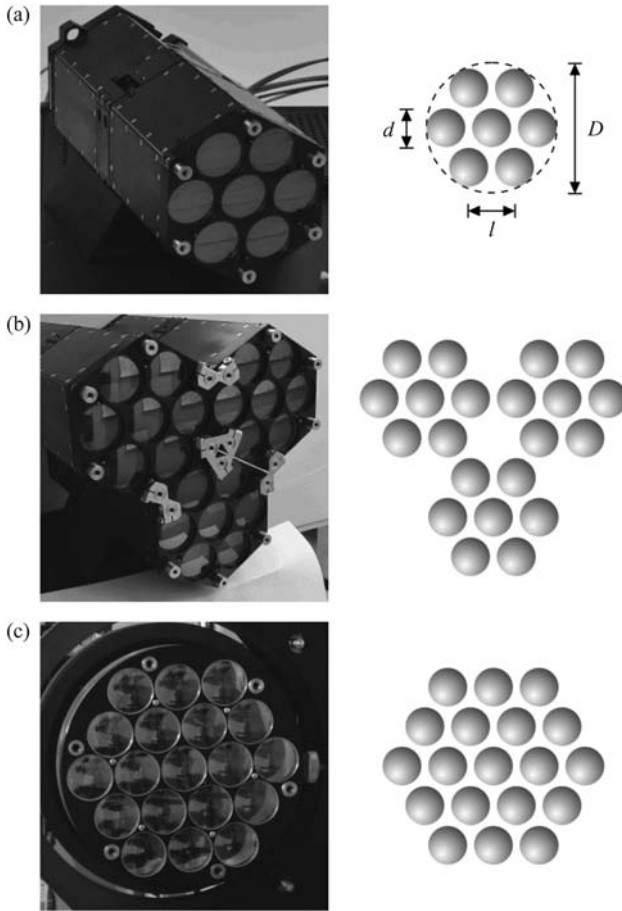


Figure 6.3 Coherent fiber array systems with (a) 7, (b) 21, and (c) 19 subapertures. In all systems, $d = 33$ mm, $l = 37$ mm, and $f_{\text{sub}} = 0.89$. The grayscale images on the right

distributions inside the subapertures. Fiber arrays in (a) and (b) are developed by Optonicus [11], and in (c) by US Army Research Laboratory.

This conclusion is further elaborated in Figure 6.5, which represents the on-axis target plane intensity values I_T^0 as functions of the propagation distance L for the fiber array transmitter geometries in Figure 6.3 with $N_{\text{sub}} = 7, 19,$ and 21 subapertures. As seen from Figure 6.5, the stair-mode approximation of the parabolic phase (dashed lines) leads to a general decrease of the target plane peak intensity value, compared to the piston and tip-tilt phase approximation (solid lines). As expected, this decrease is smaller for longer propagation distances.

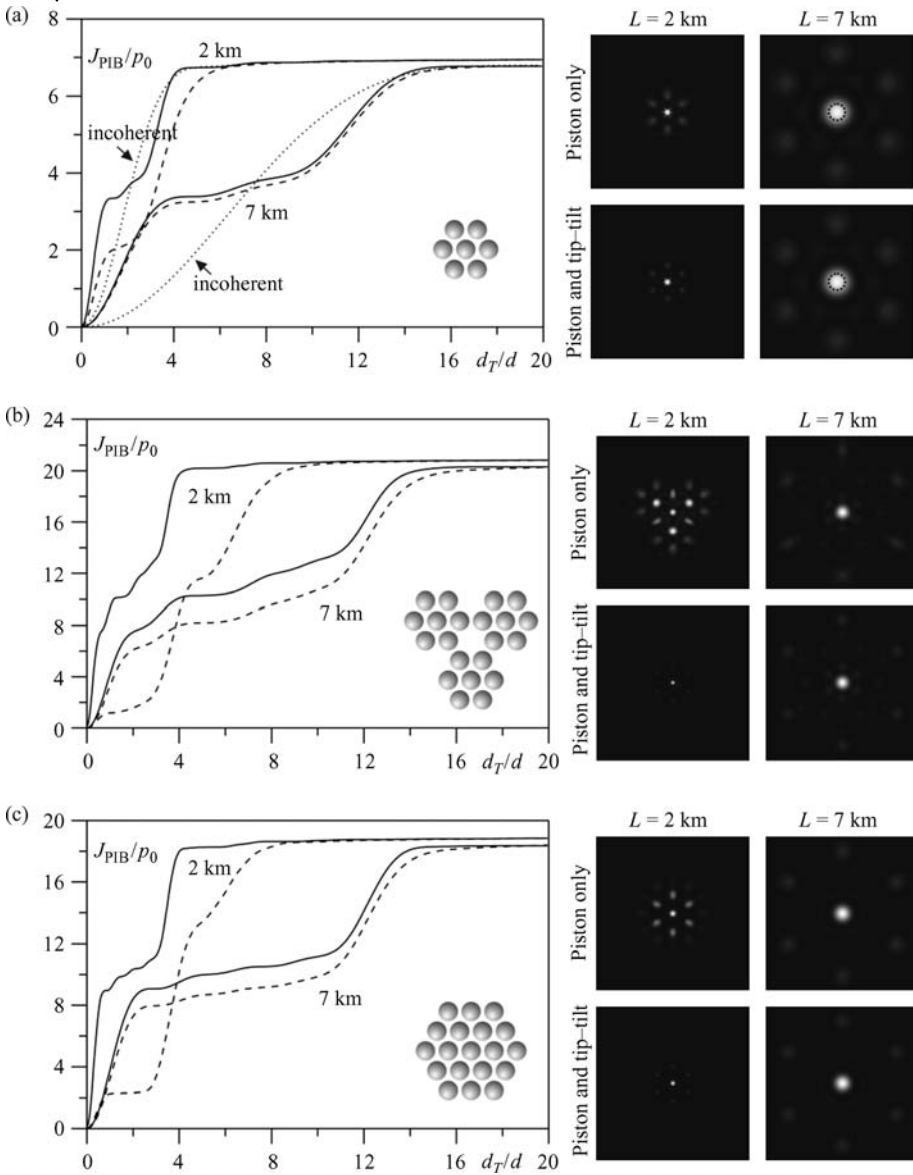


Figure 6.4 Efficiency of the target plane coherent beam combining (phase locking) over 2 and 7 km distances in vacuum for the fiber arrays in Figure 6.3 with piston and tip-tilt (solid lines) and piston-only (dashed lines) control of the outgoing beamlet phases. The PIB metric of the projected combined beam, J_{PIB} , is normalized by the power p_0 transmitted through a single-fiber array subaperture, and the on-axis bucket diameter d_T is normalized by

the fiber collimator subaperture diameter d . The tip-tilt phase components are assumed to be zero with piston-control only. Corresponding target plane intensity distributions are illustrated by the grayscale images. The dashed circles in (a) indicate the target plane receivers of diameters $d_T = 2.5$ cm for $L = 2$ km and $d_T = 5$ cm for $L = 7$ km. The dotted lines in (a) correspond to the incoherent fiber array system with seven subapertures.

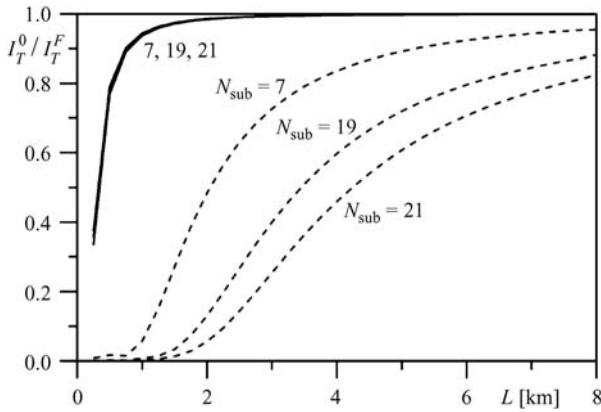


Figure 6.5 Beam projection on a remote target a distance L in vacuum for the fiber arrays in Figure 6.3 with piston and tip-tilt (solid lines) and piston-only (dashed lines) control of the outgoing beamlet phases. The on-axis target plane intensity values $I_T^0 = I_T^0(\mathbf{r} = 0)$ are normalized by the corresponding values of the on-axis target plane intensities $I_T^F = I_T^F(\mathbf{r} = 0)$ obtained using the parabolic phase inside each subaperture area.

6.3

Turbulence-Induced Phase Aberration Compensation with Fiber Array-Integrated Piston and Tip-Tilt Control

Consider now the impact of wavefront tip-tilt control at each fiber array subaperture on the mitigation of atmospheric turbulence effects. For simplicity, we assume a point source (unresolved) target at distance L in optically inhomogeneous and isotropic random medium with Kolmogorov refractive index fluctuation power spectrum (Kolmogorov turbulence model) [14]. In this commonly used model, atmospheric turbulence strength is associated with the refractive index structure parameter C_n^2 . The characteristic spatial scale of atmospheric turbulence-induced phase fluctuations at the fiber array pupil plane can be described by the Fried parameter r_0 [15] that for spherical target return wave can be represented in the form $r_0 = 3.02(k^2 C_n^2 L)^{-3/5}$, where $k = 2\pi/\lambda$, λ is the optical wavelength, and C_n^2 is assumed to be a constant along the propagation path (model for homogeneous turbulence). For estimation of the potential benefit from tip-tilt control integration into fiber collimators, assume that the outgoing beamlet phase control is based on an ideal conjugation of the measured local (subaperture-averaged) piston and tip-tilt phase components – the control approach known as *phase-conjugate aberration precompensation* [5,16,17]. In numerical simulations presented in this section, the phase conjugate control of the combined beam transmitted by the fiber array was implemented by computing the phase of the target return wave originating from a monochromatic coherent small size light source (beacon) located at the target plane. The beacon optical wave propagated through a “thin” turbulent layer (Kolmogorov’s phase screen) located near the fiber array system aperture. The local piston and

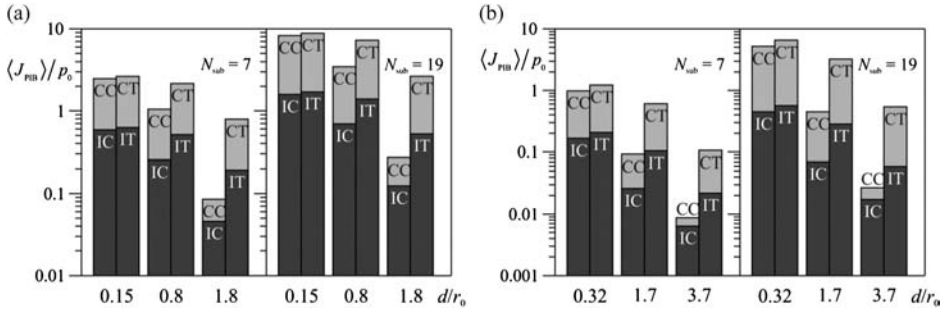


Figure 6.6 Efficiency comparison of laser beam projection using coherent (phase-locked) and incoherent fiber arrays with AO precompensation of atmospheric turbulence-induced piston and piston and tip-tilt phase aberrations using atmospheric turbulence-averaged target plane PIB metrics $\langle J_{PIB} \rangle$ for (a) 2 and (b) 7 km propagation distances and for fiber arrays with 7 and 19 subapertures. The results are obtained for the following fiber array operational modes: incoherent combining without (IC) and with (IT) tip-tilt control and

coherent combining without (CC) and with (CT) tip-tilt control. The metric values $\langle J_{PIB} \rangle$ are normalized by the power P_0 transmitted through a single fiber array subaperture. The bucket size d_T equals to $1/2$ of the diffraction-limited target plane intensity central lobe size for a coherent fiber array beam with seven subapertures ($d_T = 0.75d$ for $L = 2$ km and $d_T = 1.5d$ for $L = 7$ km, depicted by the dashed circles in Figure 6.4a). Each set of bars corresponds to different d/r_0 ratios.

tip-tilt phase turbulence-induced components were computed using decomposition of the phase screen-induced phase aberrations over Zernike polynomials inside each subaperture [18]. The obtained phase components were conjugated and used for generation of the outgoing combined beam that propagated through the same phase screen to the target plane. Compensation efficiency was estimated using the target plane PIB metric J_{PIB} . To obtain statistically averaged values of the PIB metric, computations were repeated with a set of 100 independent phase screen realizations and the obtained metric values were averaged.

The results of the system performance analysis are summarized in Figure 6.6 in the form of the target plane PIB metric bar diagrams presented in logarithmic scale. The atmospheric turbulence-averaged metric values $\langle J_{PIB} \rangle$ are compared for adaptive fiber arrays with coherent and incoherent beam combining and with and without integrated tip and tilt wavefront control capabilities. The results presented in Figure 6.6 were obtained for two different fiber arrays (with number of subapertures $N_{sub} = 7$ and 19) and for three different atmospheric turbulence conditions corresponding to $C_n^2 = 1 \times 10^{-15} \text{ m}^{-2/3}$ (weak turbulence), $1.7 \times 10^{-14} \text{ m}^{-2/3}$ (moderate turbulence), and $6 \times 10^{-14} \text{ m}^{-2/3}$ (strong turbulence). The associated d/r_0 values computed for $L = 2$ and 7 km range from $d/r_0 = 0.15$ ($L = 2$ km, weak turbulence) to $d/r_0 = 3.7$ ($L = 7$ km, strong turbulence).

The results in Figure 6.6 clearly demonstrate that for the examined system configurations, the achieved metric values are notably higher for the coherent phase-locked adaptive fiber arrays than that for the incoherent systems [compare the dark-shaded (IC) and light-shaded (CC) bars]. The gain of using the phase-locking

control increases with an increase in N_{sub} . The gain in PIB metric increase from integration of tip-tilt control appears to be insignificant for relatively weak turbulence, but grows with d/r_0 and becomes rather substantial for $d/r_0 > 1$ – compare the corresponding CC/IC and CT/IT bars. One of the most important conclusions that can be derived from the presented analysis is that under conditions of strong turbulence, the efficiency of both coherent and incoherent beam projection systems can be significantly increased by incorporating tip-tilt wavefront aberration compensation capabilities into each fiber array subaperture [5]. This integration can lead to a decrease in the required number of subapertures as well as to more efficient compensation of turbulence effects, resulting in an increase in the target hit spot brightness with even less power transmitted through the combined beam director.

It is important to point out that similar results were obtained in numerical experiments simulating laser beam projection over distributed turbulence. In these calculations, the turbulence-induced piston and tip-tilt phase control components were obtained by considering propagation of a beacon wave through a set of 10 phase screens with Kolmogorov statistics, equidistantly distributed along the propagation path. For accurate estimation of the return wave piston and tip-tilt phase components, the return field phase was unwrapped to remove 2π -phase discontinuities. The combined beam with the updated beamlet phases was propagated through the same set of phase screens to the target, where the PIB metrics were computed. However, one should note that the laser beam propagation through a distributed turbulent medium results in both intensity scintillations of the received wave and phase singularities (branch points) [19,20]. Both effects complicate computation of local piston and tip-tilt phase components.

6.4

Target Plane Phase Locking of a Coherent Fiber Array on an Unresolved Target

6.4.1

Fiber Array Control System Engineering: Issues and Considerations

In this and the following sections, we consider control algorithms and systems that can be used in fiber array-based laser beam projection systems for coherent combining at a remote target. We assume that the distance L to the target is relatively short so that the double-pass propagation delay time $\tau_{2L} = 2L/c$ (the round-trip time, where c is the speed of light) does not exceed the characteristic time τ_{at} of the atmospheric turbulence-induced refractive index inhomogeneities update inside the propagating beam footprint. This condition is typically fulfilled for the so-called tactical range distances. At this operational range, one can apply what is known as target-in-the-loop (TIL) control techniques for target plane phasing of the outgoing beamlets and atmospheric turbulence-induced aberration compensation. In the TIL phasing control concept, the target is considered as a part of the control loop in the sense that the controls applied to reshape phases of the outgoing beamlets are dependent on measurements of the backscattered (target return) wave

at the fiber array transmitter plane. Correspondingly, these measurements depend on characteristics of the target (its size, shape, surface roughness, etc.). This dependence of the backscattered wave on target characteristics significantly complicates development of TIL control techniques. To simplify the analysis, in this section we assume that the target is small in respect to the size of the diffraction-limited target plane central lobe formed by the fiber array (unresolved or point source target). In Section 6.5, we depart from this assumption and consider the more general case of an extended (resolved) target with randomly rough surface. This target type is commonly referred to as *speckle target*.

For both unresolved and resolved targets, we consider target plane fiber array phasing using the iterative control algorithm known as stochastic parallel gradient descent (SPGD) [21–23]. The SPGD control is based on optimization of a measured signal (metric) that depends on the control variables – voltages applied to either phase shifters of the MOPA system (piston phase control) or to both the phase shifters and piezoactuators of the tip–tilt control system (piston and tip–tilt control). The SPGD-based metric optimization control can result in the combined beam phasing only if the measured metric depends monotonically on the projected beam (target hit spot) quality, which is typically estimated in terms of power density or the hit spot size. In the case of a point source (unresolved) target, one can use the target return optical wave power measured inside the bistatic optical receiver aperture as the metric for the SPGD-based phase-locking control [24]. This control system is illustrated in Figure 6.1. Indeed, the measured target return wave power (PIB) monotonically depends on the transmitted beam footprint at the target plane since beamlets phasing and atmospheric turbulence effects’ mitigation lead to better energy concentration at the unresolved target. Thus, the measured PIB signal can be used as a metric for SPGD-based locking of the beamlets transmitted by the fiber array. Note that optimization of the PIB metric with SPGD control automatically results in compensation of phase shifts that are introduced by both the MOPA system and the atmospheric turbulence. Since the metric optimization process requires a number of iterations N_{it} (from tens to hundreds) [25] and each SPGD iteration takes some time τ_{it} , it is critically important that the SPGD process convergence time $\tau_{SPGD} \sim N_{it}\tau_{it}$ does not exceed the atmospheric characteristic time τ_{at} . The condition $\tau_{SPGD} < \tau_{at}$ is relatively straightforward to achieve in fiber array systems with fiber-integrated phase shifters that can operate with several gigahertz bandwidth and for propagation over relatively short distances for which the double-pass time delay $\tau_{2L} < \tau_{it} \ll \tau_{at}$ and hence can be neglected. Note that the operational frequency bandwidth of the fiber-tip positioning devices is significantly lower (on the order of a few kilohertz), which makes compensation of turbulence-induced local tip–tilt phase aberration components more challenging [7].

6.4.2

SPGD-Based Coherent Beam Combining: Round-Trip Propagation Time Issue

Assume for simplicity an unresolved target at a relatively short distance ($L < c\tau_{it}/2 \ll c\tau_{at}/2$) from a fiber array-based beam projection system and consider control of the fiber array local piston and tip–tilt phase using a SPGD metric

optimization technique. Control of the beamlets' piston phases with a conventional SPGD algorithm can be described as follows [7,23,24]. During each iteration cycle n ($n = 1, 2, 3, \dots$), the SPGD controller generates a set of small-amplitude random control voltage perturbations $\{\delta u_j^{(n)}\}$ that are superimposed with the set of piston phase control signals, $\{u_j^{(n)}\}$, where $j = 1, 2, \dots, N_{\text{sub}}$. In the simplest SPGD algorithm implementation, the perturbations represent statistically independent numbers of identical magnitude with random signs, having equal probabilities for positive and negative values. The application of signals $\{u_j^{(n)} + \delta u_j^{(n)}\}$ to the phase shifters is followed by the measurement of the performance metric value $J_+^{(n)}$ (here the PIB metric). After the metric $J_+^{(n)}$ is measured within the same n th SPGD iteration cycle, the controls with perturbations of the opposite sign $\{u_j^{(n)} - \delta u_j^{(n)}\}$ are applied to the phase shifters. This is followed by the measurement of the corresponding metric value $J_-^{(n)}$, where $J_{\pm}^{(n)} = J(u_1^{(n)} \pm \delta u_1^{(n)}, \dots, u_j^{(n)} \pm \delta u_j^{(n)}, \dots, u_{N_{\text{sub}}}^{(n)} \pm \delta u_{N_{\text{sub}}}^{(n)})$. The computed metric variation $\delta J^{(n)} = J_+^{(n)} - J_-^{(n)}$ and the applied control voltage perturbations $\{\delta u_j^{(n)}\}$ are used to generate updated control signals for the next, that is, $(n + 1)$ st iteration:

$$u_j^{(n+1)} = u_j^{(n)} + \gamma \delta J^{(n)} \delta u_j^{(n)}. \quad (6.1)$$

This control algorithm has two essential control parameters that need to be optimized: the update gain coefficient γ and the perturbation magnitude $|\delta u_j^{(n)}| = \xi = \text{const}$. Note that in more advanced SPGD control algorithms, both gain γ and perturbation magnitude ξ are automatically adjusted based on the current operation condition [26,27].

Besides control of piston phases, one can use an SPGD iterative procedure similar to Eq. (6.1) to control the outgoing beamlets' wavefront tips and tilts by applying voltages $\{v_{j,x}^{(n)}, v_{j,y}^{(n)}\}$ ($j = 1, 2, \dots, N_{\text{sub}}$) to the x - and y -actuators of the fiber positioner devices in Figure 6.2c. Since piston and tip-tilt control channels have significantly different response times ($\leq 10^{-9}$ and $\lesssim 10^{-4}$ s, respectively), the piston and tip-tilt SPGD controllers operate at considerably different iteration rates and practically do not impact each other [28–30].

The SPGD process requires precise temporal synchronization between applied controls and metric measurements, which in turn demands accounting for various delays related with finite response times of metric sensor, phase shifters, and tip-tilt actuators, the time required for computation of controls, and the round-trip propagation time delay τ_{2L} . Therefore, the SPGD controller needs to postpone its operation (to pause) for a time of duration,

$$\tau_{\text{delay}} \geq \tau_{\text{sys}} + \tau_{2L}, \quad (6.2)$$

starting from the moment when the control signals are applied, before resuming operation for metric measurement. Here, the response time τ_{sys} includes all control

system time delays mentioned above. Since in each SPGD cycle control voltages are changed twice, the characteristic SPGD iteration time τ_{SPGD} need to be at least twice as long as $\tau_{2L} + \tau_{\text{sys}}$.

For coherent beam combining over distances of about 1 km or longer, the propagation delay τ_{2L} becomes the major factor that precludes an increase of the SPGD iteration rate and thus limits the improvement of the phase-locking control convergence. For example, for a target at $L = 10$ km distance, the round-trip propagation delay is $\tau_{2L} = 66.7\mu\text{s}$, which is considerably longer than the typical control system response time, $\tau_{\text{sys}} \geq 2\mu\text{s}$. Thus, in the example considered here, the round-trip propagation delay would limit the piston phase SPGD iteration rate, $f_{\text{SPGD}} = 1/\tau_{\text{SPGD}}$, to about 7 kHz – more than 30 times less than what a commercially available multichannel SPGD controllers can achieve [11].

The propagation delay problem may be overcome using a modified SPGD algorithm (referred to here as delayed-feedback SPGD or DF-SPGD) [24,31]. In this algorithm, the controller does not need to pause during the time $\tau_{\text{delay}} \geq \tau_{\text{sys}} + \tau_{2L}$ before performing the measurement of metric signals. Instead, the control parameters update is performed using the metric values $J_+^{(n)}$ and $J_-^{(n)}$ measured without delay in connection with the perturbations $\{\delta u_j^{(n-\Delta n)}\}$, which were applied Δn iterations earlier and stored in the controller's memory.

$$u_j^{(n+1)} = u_j^{(n)} + \gamma \left[J_+^{(n)} - J_-^{(n)} \right] \delta u_j^{(n-\Delta n)}. \quad (6.3)$$

The DF-SPGD control in Eq. (6.3) requires some adjustment of parameters so that the time duration Δt between applying perturbations $\{\pm \delta u_j^{(n-\Delta n)}\}$ and the corresponding measurements of the metrics $J_{\pm}^{(n)}$ is at least $\tau_{\text{sys}} + \tau_{2L}$ and is approximately equal to $\tau_{\text{DF-SPGD}} \Delta n$, as illustrated in Figure 6.7. Correspondingly, the number Δn and the duration of a single iteration $\tau_{\text{DF-SPGD}}$ must be properly selected. Both parameters can be modified by changing the DF-SPGD controller iteration rate and duration of perturbations. Note that, in general, different combinations of Δn and $\tau_{\text{DF-SPGD}}$ can be chosen to fulfill the condition $\Delta t \cong \tau_{\text{DF-SPGD}} \Delta n$. Nevertheless, it is always desirable to keep the iteration rate as high as possible, which corresponds to using the highest Δn possible. In order to determine a proper set of parameters Δn and $\tau_{\text{DF-SPGD}}$, one needs to know the distance to the target, L , which could be determined, for example, by a target ranging system. Alternatively, a supervisory control loop could continuously adjust Δn and $\tau_{\text{DF-SPGD}}$ so that the system performance is optimized – an approach that may be applied especially in application scenarios with changing target distance.

6.4.3

Coherent Beam Combining at an Unresolved Target over 7 km Distance

In this section, we discuss practical issues related with the experimental implementation of the TIL coherent beam combining over tactical-range atmospheric paths.

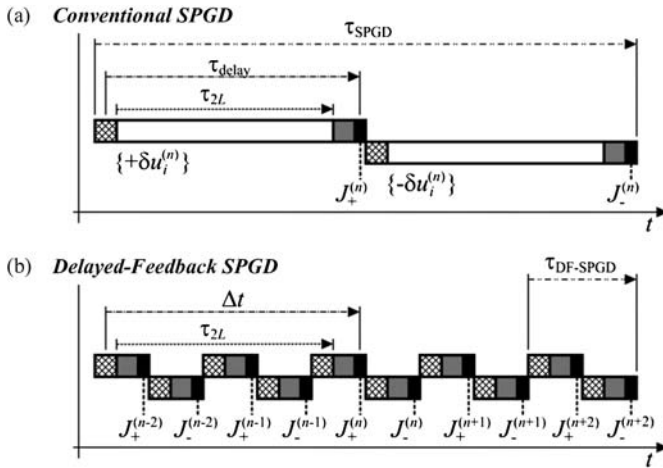


Figure 6.7 Timing diagrams for the conventional SPGD control (a) and the delayed-feedback SPGD control with $\Delta n = 2$. A single iteration indicating positive and negative perturbations is shown for conventional SPGD. In this example, utilization of the DF-SPGD control provides a fivefold increase in the iteration rate.

Experimental studies were performed using the University of Dayton’s outdoor test range. The transmitter fiber array as in Figure 6.3a and the PIB receiver were located close to a window at the Intelligent Optics Laboratory (IOL). An unresolved target (corner cube retroreflector with 50 mm diameter) was installed inside a shed on the rooftop of the Dayton VA Medical Center $L = 7$ km away from the fiber array transmitter. The propagation path profile is shown in Figure 6.8. The test range was equipped with a boundary layer scintillometer, which continuously recorded the path-averaged refractive index structure constant C_n^2 .

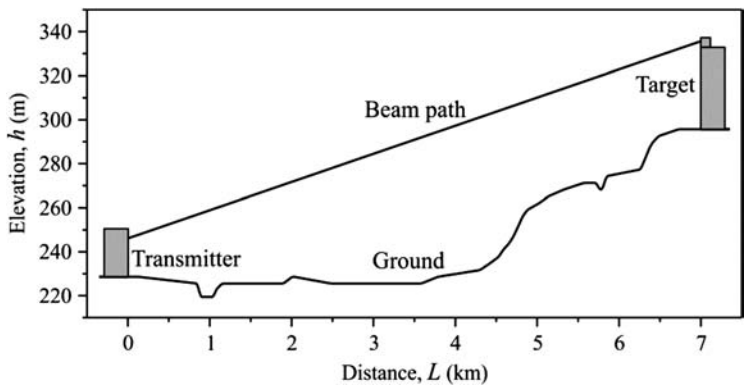


Figure 6.8 Combined laser beam 7 km long propagation path between fiber array transmitter and receiver located at the University of Dayton IOL and the retroreflector target on the rooftop of the Medical Center.

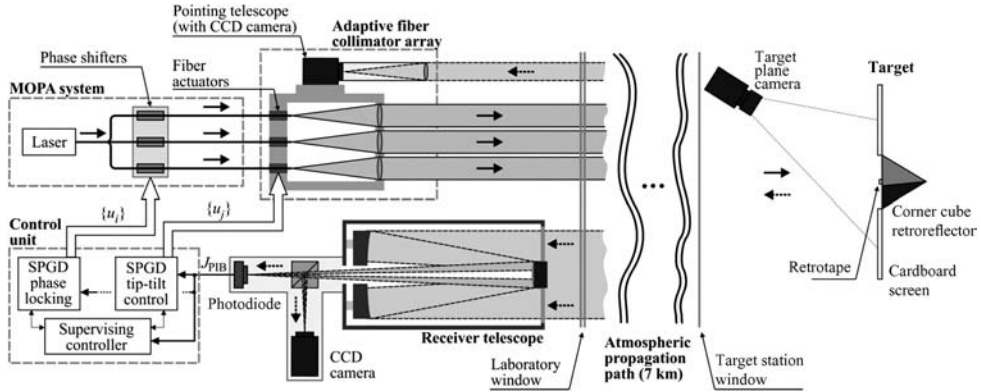


Figure 6.9 Schematic of the experimental setup used for TIL phase locking with an unresolved target over a 7 km atmospheric propagation path.

A schematic of the transmitter setup is shown in Figure 6.9. The light from a fiber-coupled laser with wavelength $\lambda = 1064$ nm and bandwidth $\Delta\nu = 5$ kHz was split into eight channels by a 1×8 fiber splitter with integrated phase shifters. Seven of the polarization-maintaining output fibers were connected to a fiber collimator array, as shown in Figure 6.3a. Each collimator was equipped with a piezoactuated fiber positioning system for control of the lateral fiber-tip position within a range of about $\pm 35 \mu\text{m}$. This corresponds to a tilt range of about ± 0.2 mrad for the aspheric collimation lenses with focal length of $f = 174$ mm [7] and results in ± 1.4 m lateral beam displacements at the target plane. The collimator array was mounted onto a gimbal together with a coboresighted small telescope, which was used to point the beams toward the target. Note that the window glass at the transmitter side introduced wavefront aberrations of about one wavelength peak-to-valley (PV) over the array aperture and $\lambda/4$ PV over a single subaperture. These aberrations were partially compensated by the subaperture tip-tilt control system.

A part of the light was reflected by the target retroreflector and propagated back to the PIB receiver based on a Schmidt-Cassegrain telescope with 20 cm aperture. A CCD camera with narrow field of view was used for the receiver telescope alignment. The receiver telescope was placed at the minimum possible distance to the collimator array. The received light power was measured by a photodetector and its output signal was used as performance metric (PIB metric, J_{PIB}) for the SPGD-based piston and tip-tilt control (Figure 6.9). The SPGD multichannel optimization controller (Optonicus, LLC) [11] was used for piston phase control (phase locking). Because the response bandwidth of the fiber actuators limits the tip-tilt control to a few kilohertz iteration rate, the corresponding control was implemented using a personal computer (PC). The two controllers operated in parallel without iteration cycles synchronization. The supervising controller (also a PC) was used to trigger the piston and tip-tilt controllers to begin or stop operation during experimental trial as well as to digitize and record metric data.

For coherent beam combining efficiency evaluation, the fiber array control system repeatedly performed sequential trials comprised of the following three stages:

Stage 1 – Feedback off: Randomized, but static, control voltages were applied to the phase shifters, tip–tilt control voltages were set to average values from previous control cycles. On average, this operational condition corresponds to incoherent beam combining.

Stage 2 – Piston control only: The SPGD controller optimized the received PIB signal by applying voltages to fiber-integrated phase shifters. For an unresolved target, this corresponds to maximization of the power within the target retro-reflector. Tip–tilt control remained off.

Stage 3 – Piston and tip–tilt phase control: Both piston and tip–tilt SPGD control systems operated in parallel.

The duration of each control phase was about 1.75 s and the trials were repeated 50 times. Values for the performance metric (received PIB), J_{PIB} , were acquired for all cycles at a sampling rate of about 10 kHz. From the measured metric data of all recorded trials, the average values $\langle J_{\text{PIB}} \rangle$ and probability distributions $\rho(J_{\text{PIB}})$ of the PIB metric values J_{PIB} were calculated for each stage separately.

Experiments were performed using either the conventional SPGD (with $\tau_{\text{SPGD}} = 130\mu\text{s}$) or the DF-SPGD control algorithms (with $\Delta n = 7$ and $\tau_{\text{SPGD}} = 7\mu\text{s}$). In Figure 6.10, the dependences $\rho(J_{\text{PIB}})$ for piston control (stage 2) with both SPGD and DF-SPGD controllers are compared with the corresponding

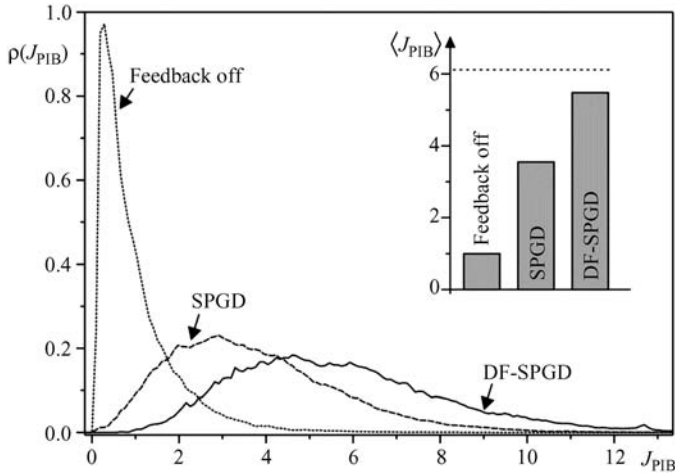


Figure 6.10 Experimental results of the coherent beam combining experiments over 7 km propagation path with an unresolved retroreflector target using the fiber array in Figure 6.3a. Measured probability densities $\rho(J_{\text{PIB}})$ for the PIB metric J_{PIB} without and with piston phase control using either the

conventional SPGD or the DF-SPGD algorithms. The inset at the right compares the corresponding average metric values $\langle J_{\text{PIB}} \rangle$. The experimental results were obtained in atmospheric turbulence conditions corresponding to $C_n^2 = 6 \times 10^{-16} \text{ m}^{-2/3}$.

dependences obtained with feedback control system off (stage 1). Coherent beam combining (phase locking) using nondelayed (conventional) SPGD control resulted in a significant increase in the observed metric values; nevertheless, as shown in Figure 6.10, utilization of the delayed SPGD control (DF-SPGD) resulted in a noticeable improvement of system performance. A comparison of average metric values, $\langle J_{\text{PIB}} \rangle$, is shown as inset in Figure 6.10. Here, all metric values were normalized to the average value measured during the feedback-off stage, that is, $\langle J_{\text{PIB}} \rangle_{(\text{Feedback off})} \equiv 1$. The average metric improvement in comparison to the uncontrolled state was 3.7 for piston phase control with the conventional SPGD and 5.6 with the DF-SPGD; the latter value corresponds to about 90% of the value 6.1 expected for vacuum propagation (indicated by a dashed line).

As seen from the probability densities $\rho(J_{\text{PIB}})$ in Figure 6.10, there were considerable fluctuations of the PIB metric J_{PIB} . However, the fluctuation level was reduced by utilizing piston phase control, which also resulted in the average metric value increase.

In the discussed phase-locking experiments, we found a negligible difference between the values of $\langle J_{\text{PIB}} \rangle$ obtained with and without subaperture tip-tilt control. This is in accordance with the discussions presented in Section 6.3, where it is shown that the impact of tip-tilt control is expected to be low for the measured relatively weak turbulence conditions (see Figure 6.6b). Moreover, the faster iteration rate of piston phase control (nearly 50-fold in case of DF-SPGD) allows a fast compensation of the overall tilt through a stair-mode approximation.

In order to verify that maximization of the PIB metric J_{PIB} indeed corresponded to a higher peak irradiance at the target, the irradiance distribution at the target plane was directly monitored. As shown in Figure 6.9, the 50 mm diameter target retroreflector was placed behind a hole of the same size in a cardboard screen. In addition, a small patch of retroreflecting tape (6 mm diameter) was attached to the center of the target retroreflector's cover glass. A camera with a wide-angle objective, placed about 1 m in front of the screen and 20 cm to the side of the line-of-sight, recorded the beam footprint on the screen at 30 frames/s. The beams at the target plane showed a considerable level of scintillations – as expected for atmospheric turbulence conditions with a Rytov variance on the order of or near unity – so a considerable frame averaging was necessary to evaluate the irradiance at the target. Figure 6.11a and b shows the center part of the target plane irradiance distributions obtained with averaging of 270 frames that were recorded while the piston phase control was off and on, respectively. The distributions clearly demonstrate the significantly higher irradiance level at the retro-reflector with TIL phase locking.

6.5

Target Plane Phase Locking for Resolved Targets

In this section we consider the case of laser beam projection onto an extended (resolved) target with randomly rough surface. The coherent beam scattering off the target's rough surface results in a strong speckle modulation at the transceiver

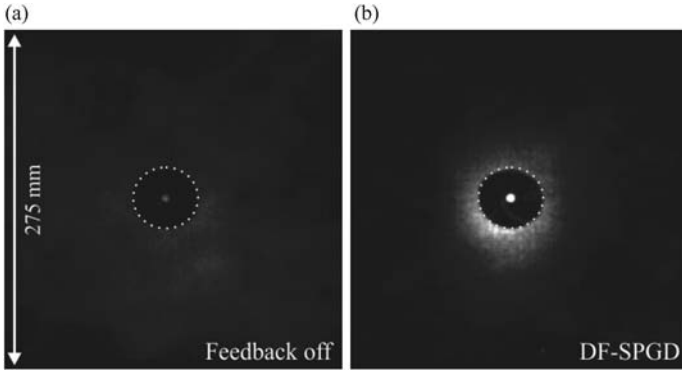


Figure 6.11 Experimental long-exposure target plane irradiance distributions in the plane of the retroreflector (a) without piston phase control, that is, with feedback off, and (b) with DF-SPGD control. The brighter spot in the center corresponds to a small patch of retroreflecting tape, which was attached to the retroreflector's cover glass. The dotted circle indicates the retro-reflector.

plane, which represents a long-standing major challenge (known from the late 1970s as the speckle problem in AO) [32–34]. We address this problem by utilizing a speckle metric optimization-based phase locking (SMPL) technique, which enabled, to our knowledge, the first successful demonstration of TIL laser beam projection onto an extended target with randomly rough surface.

6.5.1

Speckle Metric Optimization-Based Phase Locking

In the SMPL technique described here, control of the outgoing laser beam phase is performed using the optimization of speckle-averaged characteristics of the target return speckle field that are referred to here as speckle metrics [35–37]. The term “speckle averaging” implies that the return wave characteristic $J(t)$ is averaged over a time period τ_J , which exceeds significantly the characteristic time τ_{sp} needed for a speckle field realization update inside the receiver aperture. The measured characteristic $J_{sp} = \langle J \rangle_{sp}$, where $\langle \cdot \cdot \cdot \rangle_{sp}$ denotes speckle averaging, can be utilized for phase-locking control as a performance measure (speckle metric) if the following conditions are fulfilled: (i) J_{sp} depends monotonically on a target plane beam quality metric J_T , which characterizes the power density distribution inside the target hit spot, and (ii) J_{sp} can be measured over a time τ_J that is considerably shorter than the characteristic times τ_{at} and τ_{AO} of turbulence and closed-loop phase control, respectively. From condition (ii) follows a hierarchy of characteristic time scales that is required for SMPL control implementation:

$$\tau_{sp} \ll \tau_J \ll \tau_{AO} \leq \tau_{at}. \quad (6.4)$$

To estimate the upper limit for the characteristic time for speckle realization updates, τ_{sp} , assume in Eq. (6.4) that $\tau_{sp} \approx 10^{-2}\tau_J \approx 10^{-4}\tau_{at}$. With a common

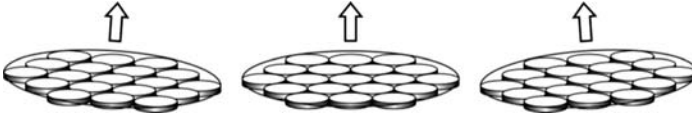


Figure 6.12 Illustration of wavefront phase tilt control using subaperture piston phases (stair-mode approximation of wavefront tilt aberration).

estimate for the characteristic atmospheric time $\tau_{\text{at}} = 1$ ms, we obtain $\tau_{\text{sp}} = 0.1\mu\text{s}$. Note that this condition can be naturally fulfilled only for extremely fast spinning targets. Therefore, in the SMPL technique described here, the fast speckle field realization update that is required for speckle metric measurements is generated by artificially induced hit spot dithering, achieved by modulating the outgoing combined beam's wavefront tip and tilt. Because this tip-tilt phase modulation with hit spot dithering frequencies $\omega_{\text{dith}} \sim 1/\tau_{\text{sp}}$ in the 10 MHz range cannot be achieved using conventional optomechanical beam-steering mirrors, in the SMPL approach the required high-frequency hit spot dithering is obtained using a piston-wise (stair-mode) approximation of the outgoing beam wavefront tilts, as illustrated in Figure 6.12. Since this dithering can be performed using fiber-integrated phase shifters with bandwidths in the gigahertz range, the condition for τ_{sp} in Eq. (6.4) can easily be fulfilled.

Note that dithering of the outgoing beam also results in an undesired overall increase of the projected beam's long-exposure hit spot footprint and the corresponding decrease of the time-averaged power density. For this reason, the stair-mode dithering amplitude should be small, but still large enough to provide a statistically representative ensemble of uncorrelated (or at least weakly correlated) speckle field realizations that can be used for speckle metric evaluation. A small dithering amplitude is also important for mitigation of anisoplanatic effects [38]. As analysis and experiments show, the hit spot dithering with amplitudes of 75–100% of the diffraction-limited beam size represents an acceptable compromise between the factors already mentioned [38].

6.5.2

Speckle Metrics

In this section we show that processing of the PIB signal $J_{\text{PIB}}(t)$ measured with a receiver telescope (PIB receiver) allows obtaining speckle metrics J_{sp} that can be utilized for SMPL in the beam projection system depicted in Figure 6.1. The speckle metrics considered here are derived from an analysis of the temporal correlation function of the time-varying (AC) component $\delta J_{\text{PIB}}(t)$ of the measured PIB signal $J_{\text{PIB}}(t)$: $\Gamma_{\text{PIB}}(\tau) \equiv \langle \delta J_{\text{PIB}}(t) \delta J_{\text{PIB}}(t + \tau) \rangle_{\text{sp}}$.

Consider laser beam projection in an optically homogeneous medium onto a flat randomly rough target surface and assume that the characteristic roughness correlation distance l_s and roughness root-mean-square (rms) amplitude σ_s are significantly smaller than the hit spot size b_s , but larger than the transmitted beam

wavelength λ . In the case of the hit spot dithering with velocity \mathbf{v}_s at the target, one can obtain the following relationship between correlation function $\Gamma_{\text{PIB}}(\tau)$ and the target plane intensity distribution $I_T(\mathbf{r})$ [35,37]:

$$\Gamma_{\text{PIB}}(\tau) = C \int I_T(\mathbf{r}) I_T(\mathbf{r} + \mathbf{v}_s \tau) d^2 \mathbf{r}, \quad (6.5)$$

where C is a constant. We assumed here that $\sigma_s \geq l_s$ (very rough surfaces) and that the receiver aperture D_R exceeds the characteristic speckle size a_{sp} . The dependence described by Eq. (6.5) can be utilized for derivation of a set of different speckle metrics. Consider first the PIB signal fluctuation variance that can be obtained by substituting $\tau = 0$ into Eq. (6.5):

$$\sigma_{\text{PIB}}^2 = \Gamma_{\text{PIB}}(0) = \langle \delta J_{\text{PIB}}^2 \rangle = C \int I_T^2(\mathbf{r}) d^2 \mathbf{r}. \quad (6.6)$$

From Eq. (6.6) follows that σ_{PIB}^2 is proportional to the sharpness function $J_2 = \int I_T^2(\mathbf{r}) d^2 \mathbf{r}$ – the target plane metric that is widely used for characterization of image and hit spot quality [39]. The relationship (6.6) shows that σ_{PIB}^2 can be considered as a speckle metric whose maximization results in an increase of the J_2 metric.

The PIB fluctuation power spectrum $G_{\text{PIB}}(\omega)$ offers another possibility for defining speckle metrics [35,40]. Using the Wiener–Khinchin theorem, from Eq. (6.5) we get

$$G_{\text{PIB}}(\omega) = \frac{C}{\pi} \int_0^\infty \int \cos(\omega \tau) I_T(\mathbf{r}) I_T(\mathbf{r} + \mathbf{v}_s \tau) d^2 \mathbf{r} d\tau. \quad (6.7)$$

For a Gaussian beam $I_T(\mathbf{r})$ of width b_s , one can obtain from Eq. (6.7) the following analytical expression for $G_{\text{PIB}}(\omega)$:

$$G_{\text{PIB}}(\omega) = G_{\text{PIB}}(0) \exp(-\omega^2 / \omega_{\text{PIB}}^2), \quad (6.8)$$

where $\omega_{\text{PIB}} = |\mathbf{v}_s|/b_s$ is the characteristic frequency bandwidth of PIB signal fluctuations [35,40,41]. The bandwidth monotonically increases with decreasing hit spot size b_s . This dependence of the PIB signal power spectrum on the hit spot size suggests that changes in the hit spot size impact the power spectrum components and can be evaluated by band-pass filtering of the PIB signal. The corresponding signals

$$P(\omega_j, \Delta_j) = \int_{\omega_j - \Delta_j/2}^{\omega_j + \Delta_j/2} G_{\text{PIB}}(\omega) d\omega \quad (6.9)$$

or their various combinations can be used to define speckle metrics of the type

$$J_{\text{sp}} = \sum_{j=1}^N \beta_j P(\omega_j, \Delta_j), \quad (6.10)$$

where $j = 1, \dots, N$ denotes a number of band-pass filters with central frequencies $\{\omega_j\}$ and bandwidths $\{\Delta_j\}$, and $\{\beta_j\}$ are weighting coefficients [35,37,40]. In contrast

to the speckle metric σ_{PIB}^2 from Eq. (6.6), the power spectrum frequency components below $\omega_1 - \Delta_1/2$ and higher than $\omega_N + \Delta_N/2$ do not contribute to the spectral speckle metric, as defined by Eqs. (6.9) and (6.10). Control of the parameters $\{\omega_j\}$, $\{\Delta_j\}$, and $\{\beta_j\}$ in Eq. (6.10) allows optimization of the speckle metric's dependence on the target hit spot intensity distribution.

Contrary to the speckle metric σ_{PIB}^2 , whose value is directly associated with the target plane metric J_2 , a similar type of analytical expression linking the speckle metric defined in Eq. (6.6) with a physically meaningful target plane metric is not available. Nevertheless, both experiments and numerical simulations show that with a correct selection of parameters in Eq. (6.10), the obtained PIB signal characteristic can be used as a speckle metric, where its global maximum corresponds to the undistorted hit spot beam intensity distribution [42,43].

Note that even though the speckle metrics defined in Eqs. (6.6) and (6.10) are obtained for speckle field propagation in vacuum, it was shown that, at least in weak and medium-strength atmospheric turbulence conditions, turbulence has a relatively small impact on the speckle field statistical characteristics and the dependence of the speckle metrics on the target hit spot size is practically unchanged [43]. This property of the speckle field forms the physical basis for the use of the SMPL for beam projection systems operating in atmospheric turbulence conditions.

6.5.3

Experimental Evaluation of Speckle Metric-Based Phase Locking

For experimental validation of speckle metric sensing and speckle metric-based coherent beam combining, a series of laboratory benchtop experiments were performed using a fiber collimator array with seven subapertures. A notional schematic of the experimental setup is shown in Figure 6.13. The transmitted collimated beamlets emerging from the fiber array system were focused by a lens.

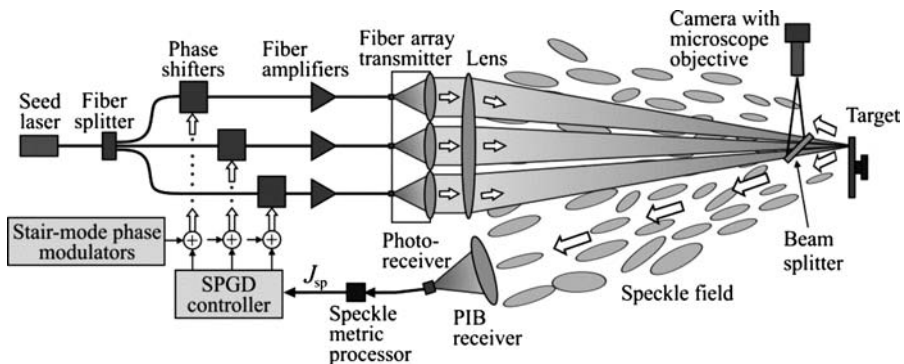


Figure 6.13 Notional schematic of the experimental setup for evaluation of speckle metric-based coherent beam combining at an extended target.

The converging combined beam was split by a beam splitter into two legs. The extended target was located in the focal plane of the first leg, while in the second leg a CCD camera (with an attached microscope objective) recorded the irradiance distribution at a plane conjugate to the target surface plane. Part of the scattered light (speckle field) was picked up by the PIB receiver, which comprised a lens with a photodetector placed at the location of the target hit spot's image formed by the receiver lens. The photodetector's output signal, the PIB metric $J_{\text{PIB}}(t)$, was proportional to the scattered wave power incident to the PIB receiver aperture. The speckle metric processor computed the PIB metric's standard deviation σ_{PIB} using an analogue circuit with an integration time $\tau_j \approx 1\mu\text{s}$. The signal $J_{\text{sp}} = \sigma_{\text{PIB}}$ was used by the SPGD controller as the speckle metric [44].

As shown in Figure 6.13, in each control channel, the output signal of the SPGD controller was mixed with a stair-mode modulation signal of 50 MHz frequency. The amplitudes and phases of the modulation signals were set as to provide a linear tilt dithering (stair-mode steering) of the outgoing combined beam. The amplitude of the linear displacement of the target hit spot was about $20\mu\text{m}$, which approximately corresponds to the diffraction-limited size of the central lobe of the fiber collimator array's far-field irradiance pattern.

Figure 6.14 shows the target plane irradiance distributions, which were recorded with the CCD camera under different operational conditions of the coherent beam combining system. Random piston phases with both SPGD controller and stair-mode dithering off resulted in the irradiance distribution of Figure 6.14a. SPGD

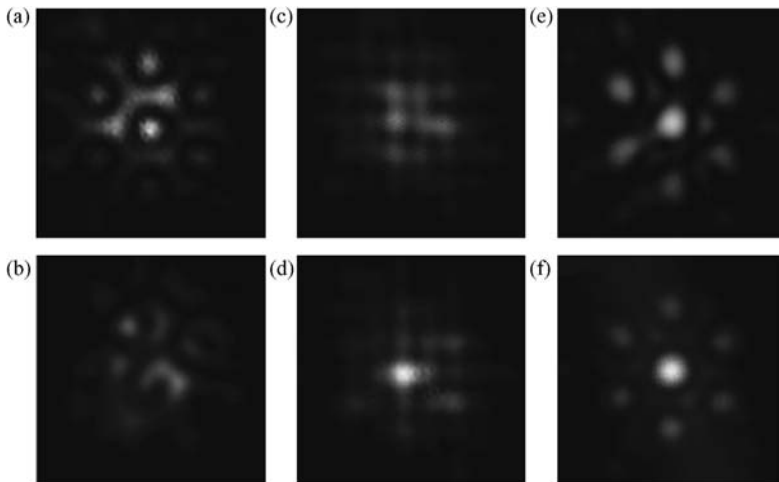


Figure 6.14 Intensity patterns at the randomly rough target surface (in the experimental setup shown in Fig. 6). (a) No phase control. (b) TIL SPGD phase control using the PIB metric with a resolved target. (c) Uncontrolled phase with stair-mode beam dithering on. (d) TIL SMPL

with resolved target using hit spot dithering. (e) TIL SMPL with a rotating resolved target without dithering. (f) SPGD phase locking with an unresolved target. The side length of each panel corresponds to about $170\mu\text{m}$.

optimization of the PIB metric J_{PIB} – a setting conventionally used for beam combining on an unresolved target – resulted in the irradiance pattern of Figure 6.14b, which clearly indicates random relative phases of the beamlets. Figure 6.14c depicts the target plane when the beamlet phases were not controlled, while the stair-mode modulation signals were applied to the phase shifters. The dithering caused a reduction of the contrast of the interference pattern. The irradiance pattern resulting from phase locking using SPGD-based maximization of the speckle metric, $J_{\text{sp}} = \sigma_{\text{PIB}}$, with stair-mode beam steering is shown in Figure 6.14d. In contrast to PIB metric optimization, SMPL with SPGD optimization resulted in an increase of the projected beam’s power density at the extended target with about twofold increase of the average hit spot peak irradiance.

The experimental setup was also used to evaluate SMPL without the hit spot dithering, but with a target rotating at about 100 revolutions per second. In this case the dynamics of the speckle pattern was much slower and to enable phase control, the integration time τ_j for speckle metric measurements and the SPGD controller’s iteration time τ_{iter} had to be increased by more than three orders of magnitude. This was still sufficient to compensate for the random piston phases inherent to the MOPA and fiber optical systems. The resulting target plane intensity pattern, which is shown in Figure 6.14e, was close to the pattern observed with a PIB metric and an unresolved target (shown for comparison in Figure 6.14f). These results clearly indicate that the SMPL technique indeed offers a path toward TIL phase locking for laser beam projection on an extended target with randomly rough surface.

6.6 Conclusion

In this chapter, we considered coherent beam combining using different configurations of fiber array-based laser transmitters with integrated capabilities for piston and tip–tilt phase control at each fiber collimator aperture. In the TIL experiments over a 7 km atmospheric propagation path, it was demonstrated that SPGD-based adaptive control of the piston and the tip and tilt phases at each fiber collimator results in automatic focusing of the combined beam onto an unresolved target with precompensation of atmospheric turbulence-induced phase aberrations. The system performance was significantly increased by using an SPGD control that accounts for the round-trip propagation delay (delayed-feedback SPGD).

A new adaptive optics control technique that allows coherent beam combining at an extended (speckle) target was described. This control technique is based on SPGD optimization of the target return speckle field’s statistical characteristics – speckle metrics. A characteristic feature of speckle metrics is their monotonic dependence on the high-energy laser beam power density inside the target hit spot. In the experiments, the speckle metric sensing was achieved by utilizing a megahertz-rate beam dithering with a stair-mode approximation of

the outgoing combined beam's wavefront tip and tilt with subaperture piston phases. Fiber-integrated phase shifters were used for both the stair-mode beam dithering and speckle metric optimization with the SPGD control technique.

Acknowledgments

This work was supported in part through cooperative agreements between the U.S. Army Research Laboratory (ARL) and the University of Dayton as well as between ARL and Optonicus, LLC.

References

- 1 Leger, J.R., Nilsson, J., Huignard, J.-P., Napartovich, A.P., Shay, T.M., and Shirakawa, A. (2009) Special issue on laser beam combining and fiber laser systems. *IEEE J. Sel. Top. Quantum Electron.*, **15**, 237–470.
- 2 Wagner, T.J. (2012) Fiber laser beam combining and power scaling progress: Air Force Research Laboratory Laser Division. *Proc. SPIE*, **8237**, 823718-1–1823718-9.
- 3 Fan, T.Y. (2005) Laser beam combining for high-power, high-radiance sources. *IEEE J. Sel. Top. Quantum Electron.*, **11**, 567–577.
- 4 Vorontsov, M.A. and Lachinova, S.L. (2008) Laser beam projection with adaptive array of fiber collimators: I. Basic considerations for analysis. *J. Opt. Soc. Am. A*, **25**, 1949–1959.
- 5 Lachinova, S.L. and Vorontsov, M.A. (2008) Laser beam projection with adaptive array of fiber collimators: II. Analysis of atmospheric compensation efficiency. *J. Opt. Soc. Am. A*, **25**, 1960–1973.
- 6 Sprangle, P., Ting, A., Penano, J., Fischer, R., and Hafizi, B. (2009) Incoherent combining and atmospheric propagation of high-power fiber lasers for directed-energy applications. *IEEE J. Quantum Electron.*, **45**, 138–148.
- 7 Vorontsov, M.A., Weyrauch, T., Beresnev, L.A., Carhart, G.W., Liu, L., and Aschenbach, K. (2009) Adaptive array of phase-locked fiber collimators: analysis and experimental demonstration. *IEEE J. Sel. Top. Quantum Electron.*, **15**, 269–280.
- 8 Vorontsov, M.A. and Kolosov, V.V. (2005) Target-in-the-loop beam control: basic considerations for analysis and wave-front sensing. *J. Opt. Soc. Am. A*, **22**, 126–141.
- 9 Valley, M.T. and Vorontsov, M.A. (eds) (2004) *Target-in-the-Loop: Atmospheric Tracking, Imaging, and Compensation*, Proceedings of SPIE, vol. 5552, Society of Photo Optical, Bellingham, WA.
- 10 Beresnev, L.A. and Vorontsov, M.A. (2005) Design of adaptive fiber optics collimator for free-space communication laser transceiver. *Proc. SPIE*, **5895**, 58950R-1–58950R-7.
- 11 Optonicus (2012) <http://www.optonicus.com>, August 17.
- 12 Born, M. and Wolf, E. (1980) *Principles of Optics*, 6th edn, Pergamon Press, New York.
- 13 Goodman, J.W. (1996) *Introduction to Fourier Optics*, 2nd edn, McGraw-Hill, New York.
- 14 Kolmogorov, A.N. (1941) The local structure of turbulence in incompressible viscous fluid for very large Reynolds numbers. *Dokl. Akad. Nauk SSSR*, **30**, 299–303 (English translation in *Turbulence: Classic Papers on Statistical Theory*, eds S.K. Friedlander and L. Topper, Interscience, New York, 1961, pp. 151–155).
- 15 Fried, D.L. (1966) Optical resolution through a randomly inhomogeneous medium for very long and very short exposures. *J. Opt. Soc. Am.*, **56**, 1372–1379.

- 16 Tyson, R.K. (1997) *Principles of Adaptive Optics*, 2nd edn, Academic Press, Boston, MA.
- 17 Vorontsov, M.A., Kolosov, V.V., and Kohnle, A. (2007) Adaptive laser beam projection on an extended target: phase- and field-conjugate precompensation. *J. Opt. Soc. Am. A*, **24**, 1975–1993.
- 18 Noll, R.J. (1976) Zernike polynomials and atmospheric turbulence. *J. Opt. Soc. Am.*, **66**, 207–211.
- 19 Fried, D.L. and Vaughn, J.L. (1992) Branch cuts in the phase function. *Appl. Opt.*, **31**, 2865–2882.
- 20 Fried, D.L. (1998) Branch point problem in adaptive optics. *J. Opt. Soc. Am. A*, **15**, 2759–2768.
- 21 Vorontsov, M.A. and Sivokon, V.P. (1998) Stochastic parallel-gradient-descent technique for high-resolution wave-front phase-distortion correction. *J. Opt. Soc. Am. A*, **15**, 2745–2758.
- 22 Vorontsov, M.A., Carhart, G.W., and Ricklin, J.C. (1997) Adaptive phase-distortion correction based on parallel gradient-descent optimization. *Opt. Lett.*, **22**, 907–909.
- 23 Vorontsov, M.A., Carhart, G.W., Cohen, M., and Cauwenberghs, G. (2000) Adaptive optics based on analog parallel stochastic optimization: analysis and experimental demonstration. *J. Opt. Soc. Am. A*, **17**, 1440–1453.
- 24 Weyrauch, T., Vorontsov, M.A., Carhart, G.W., Beresnev, L.A., Rostov, A.P., Polnau, E.E., and Liu, J.J. (2011) Experimental demonstration of coherent beam combining over a 7km propagation path. *Opt. Lett.*, **36**, 4455–4457.
- 25 Liu, L., Vorontsov, M.A., Polnau, E., Weyrauch, T., and Beresnev, L.A. (2007) Adaptive phase-locked fiber array with wavefront phase tip-tilt compensation using piezoelectric fiber positioners. *Proc. SPIE*, **6708**, 67080K-1–67080K-12.
- 26 Vorontsov, M.A., Riker, J., Carhart, G.W., Gudimetla, V.S.R., Beresnev, L.A., Weyrauch, T., and Roberts, L.C. (2009) Deep turbulence effects compensation experiments with a cascaded adaptive optics system using a 3.63m telescope. *Appl. Opt.*, **48**, A47–A57.
- 27 Weyrauch, T. and Vorontsov, M.A. (2005) Atmospheric compensation with a speckle beacon in strong scintillation conditions: directed energy and laser communication applications. *Appl. Opt.*, **44**, 6388–6401.
- 28 Vorontsov, M.A. and Carhart, G.W. (2006) Adaptive wavefront control with asynchronous stochastic parallel gradient descent clusters. *J. Opt. Soc. Am. A*, **23**, 2613–2622.
- 29 Weyrauch, T. and Vorontsov, M.A. (2004) Free-space laser communications with adaptive optics: atmospheric compensation experiments. *J. Opt. Fiber Commun. Rep.*, **1**, 355–379.
- 30 Weyrauch, T., Liu, L., Vorontsov, M.A., and Beresnev, L.A. (2004) Atmospheric compensation over a 2.3 km propagation path with a multi-conjugate (piston-MEMS/modal DM) adaptive system. *Proc. SPIE*, **5552**, 73–84.
- 31 Vorontsov, M.A. and Carhart, G.W. (2011) *Iteration Rate Improvement for SPGD Procedure, Invention Disclosure*, U.S. Army Research Laboratory.
- 32 Pearson, J.E., Kokorowski, S.A., and Pedinoff, M.E. (1976) Effects of speckle in adaptive optical systems. *J. Opt. Soc. Am.*, **66**, 1261–1267.
- 33 Vorontsov, M.A., Karnaukhov, V.N., Kuz'minskii, A.L., and Shmal'gauzen, V.I. (1984) Speckle effects in adaptive optical systems. *Kvant. Elektron.*, **11**, 1128–1137 (English translation in *Sov. J. Quantum Electron.* (1984) **14**, 761–766).
- 34 Piatrou, P. and Roggemann, M. (2007) Beaconless stochastic parallel gradient descent laser beam control: numerical experiments. *Appl. Opt.*, **46**, 6831–6842.
- 35 Vorontsov, M.A. and Shmal'hauzen, V.I. (1985) *Principles of Adaptive Optics*, Nauka, Moscow.
- 36 Vorontsov, M.A. and Carhart, G.W. (2002) Adaptive phase distortion correction in strong speckle-modulation conditions. *Opt. Lett.*, **27**, 2155–2157.
- 37 Vorontsov, M.A. (2004) Target in the loop propagation in random media. Technical Report 2004/22, FGAN FOM, Germany.
- 38 Vorontsov, M.A., Kolosov, V.V., and Polnau, E. (2009) Target-in-the-loop wavefront sensing and control with a Collett–Wolf

- beacon: speckle-average phase conjugation. *Appl. Opt.*, **48**, A13–A19.
- 39 Muller, R.A. and Buffington, A. (1974) Real-time correction of atmospherically degraded telescope images through image sharpening. *J. Opt. Soc. Am.*, **64**, 1200–1210.
- 40 Vorontsov, M.A., Carhart, G.W., Pruidze, D.V., Ricklin, J.C., and Voelz, D.G. (1996) Image quality criteria for an adaptive imaging system based on statistical analysis of the speckle field. *J. Opt. Soc. Am. A*, **13**, 1456–1466.
- 41 Goldfischer, L.I. (1965) Autocorrelation function and power spectral density of laser-produced speckle patterns. *J. Opt. Soc. Am.*, **55**, 247–253.
- 42 Deng, Y., Cauwenberghs, G., Polnau, E., Carhart, G., and Vorontsov, M. (2005) Integrated analog filter bank for adaptive optics speckle field statistical analysis. *Proc. SPIE*, **5895**, 58950L-1–58950L-9.
- 43 Dudorov, V.V., Vorontsov, M.A., and Kolosov, V.V. (2006) Speckle-field propagation in “frozen” turbulence: brightness function approach. *J. Opt. Soc. Am. A*, **23**, 1924–1936.
- 44 Vorontsov, M., Weyrauch, T., Lachinova, S., Gatz, M., and Carhart, G. (2012) Speckle-metric-optimization-based adaptive optics for laser beam projection and coherent beam combining. *Opt. Lett.*, **37**, 2802–2804.

